Research Article Vol. 38, No. 10 / October 2021 / Journal of the Optical Society of America B 2823

Journal of the Optical Society of America B

OPTICAL PHYSICS

Multifunctional Fano resonance modulator with graphene-based double-layer independent gratings

WENJIE SHI,[1] YIQING WANG,[1] JIACHENG ZHOU,[1] ZHENGDA HU,[1] JICHENG WANG,[1,2] AND LIFA HU[1,*]

[1]School of Science, Jiangsu Provincial Research Center of Light Industrial Optoelectronic Engineering and Technology, Jiangnan University, Wuxi 214122, China

[2]State Key Laboratory of Applied Optics, Changchun Institute of Optics, Fine Mechanics and Physics, Chinese Academy of Sciences, Changchun 130033, China

*Corresponding author: hulifa@jiangnan.edu.cn

Received 25 May 2021; revised 16 August 2021; accepted 16 August 2021; posted 17 August 2021 (Doc. ID 432347); published 10 September 2021

Fano resonance is based on a plasmonic metasurface and has many applications in various fields. In this paper, we propose an independently adjustable graphene-based double-layer grating structure. We control multiple Fano resonances at different wavelengths and bandwidths by regulating the Fermi level thanks to the preeminent characteristic of graphene. Here, the equivalent resonator coupled-mode method is used to better describe the Fano resonance of this designed structure adequately, and the transmission spectra fit well. The functional switch could be achieved at different wavelengths by using Fano resonance. We can obtain excellent group refractive index of this designed structure, which means it has superior applications in slow light. The effect of the refractive index of the dielectric layer on the sensing performance is researched so that the structure has a good application in sensors. Furthermore, we look forward to making potential contributions to fabricate integrated optical sensors and devices based on those elaborately designed structures.

https://doi.org/10.1364/JOSAB.432347

1. INTRODUCTION

Fano resonance was originally a quantum interference phenomenon produced by discrete and continuous states in atomic physic [1,2]. Researchers have found that Fano resonance is also widespread in optical systems. Fano resonance is formed by the interference of discrete states (or narrow resonance modes) and continuous states (or wide resonance modes). In addition, a surface plasmon [3–5] is an electromagnetic wave generated by interacting freely vibrating electrons and photons at the metal–dielectric interface, which have strong enhancement of the local electric field and much better adaptability to nanoarchitectures. This common optical phenomenon has many applications in metallic systems, such as photodetectors [6], optical switches [7], and optical absorbers [8], and plasmon-induced transparency (PIT). The PIT is a special Fano resonance. It can be achieved by the coupling of bright–dark mode and bright–bright mode [9–11]. Fano resonance has been widely used in various types of systems, including optical filtering [12], slow-light propagation [13], and sensors [14].

The Fano resonance can be achieved in metal or dielectric metamaterial structures. Since metal or dielectric metamaterial structures are difficult to modify after manufacturing, their adjustment efficiency is low, and the wavelength tuning range is restricted, Fano resonance can only work within a preset frequency band or resonance frequency. One key advantage of graphene [15,16] surface plasmons is that they can control optical responses by adjusting gating techniques, an external magnetostatic field, chemical potential [17]. The grating can be regarded as one of the simplest metamaterials in the grating-coupling device, metal, or semiconductor [18]. When the electromagnetic wave is incident on the grating, the electromagnetic wave that meets the wave-vector-matching condition will have a strong interaction with the grating, stimulating the plasmon resonance. Kim *et al.* in 2016 proposed a subwavelength grating with a mixed structure of gold and graphene strips on a silicon nitride substrate [19]. The super transmission effect of infrared waves was achieved. Then, Yang *et al.* developed an SiC grating with perfect absorption and strong magnetic polaritons [20]. The surface plasmons excited at the double orthogonal grating and dynamically tunable PIT were achieved in 2018 [21]. Furthermore, Bai *et al.* proposed a graphene grating and achieved a TE/TM mode switch [22].

In this study, we have designed a graphene double grating (GDG) hybrid system that is independently flexible. The

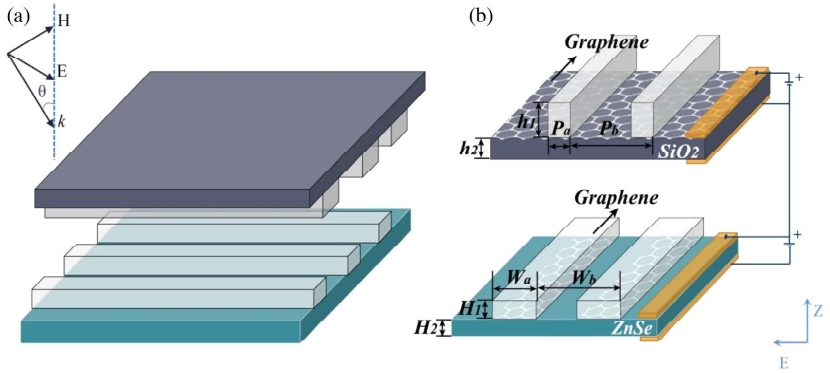

Fig. 1. (a) 3D schematic illustration of the GDG; (b) diagrammatic sketch of one period with the geometric parameters $P_a = 70$ nm, $W_a = 60$ nm, $P_b = 120$ nm, $W_b = 120$ nm, $h_1 = 80$ nm, $h_2 = 50$ nm, $H_1 = 100$ nm, and $H_2 = 50$ nm, respectively. The Fermi levels of UGG and LGG can be adjusted simultaneously by imposing two independent bias voltages between the two gold gates and the conductive gap.

numerical simulation of the GDG's optical properties results in superior Fano resonance and related applications. This structure is composed of two graphene gratings made of different materials. By optimizing the double-layer grating and graphene geometric parameters, respectively, we were able to achieve the desired performance. Through theoretical analysis of coupled-mode theory (CMT), we discovered that the theoretical fitting results can match the simulated numerical data. The structure can also be given potential in near-field optical switching due to the advantages of Fano resonance. Through the group refractive index data, we know that the GDG has excellent slow-light capability. A high-quality sensor can be achieved due to the high sensitivity and the figure of merit (FOM).

2. STRUCTURE AND THEORY

Figure 1 displays a GDG hybrid system to investigate the Fano resonance. A dielectric spacer separates two graphene gratings. The periodic structure is made up of three constituent elements: a graphene upper grating (bright mode) with the Fermi level, graphene lower grating (bright mode) with Fermi level dielectric spacer. COMSOL Multiphysics was utilized to perform the numerical simulation in this article, which was done using finite-element methods. Silica and ZnSe are believed to have upper graphene grating (UGG) and lower graphene grating (LGG) in the simulation. The dielectric constants of these two materials are 3.9 [23] and 2.4 [24], respectively. We use periodic boundary conditions in both x and y directions in our simulations. While broadband plane waves are incident from the z direction, we apply a perfectly matched layer along the z direction to absorb all light reaching the boundary. The graphene model is constructed as a surface current boundary condition. The TM-polarized wave is incident in the negative direction of the z axis. The Kubo formula derived from the random phase approximation has the surface conductivity of single-layer graphene [25–27] according to theoretical and experimental research,

$$\sigma_g = \frac{ie^2 E_f}{\pi\hbar^2\left(\omega + i\tau^{-1}\right)}. \tag{1}$$

Here, ω is the angular frequency, E_f is the Fermi energy, and $\hbar$ is the reduced Planck constant. The intrinsic relaxation time is represented as $\tau = E_f\mu/e\upsilon_F^2$, where $\upsilon_F \approx 10^6$ m/s is the Fermi velocity and μ is the carrier mobility. Based on previous research, the mobility of graphene films can reach up to 40,000 $\mathrm{cm^2V^{-1}s^{-1}}$ at room temperature [28,29]. Thus, μ used in this paper is 15,000 $\mathrm{cm^2V^{-1}s^{-1}}$, which is an appropriate choice considering the feasibility of practical submissions.

The energy can be coupled into the GDG with the incidence of TM-polarized waves, and the dynamic transmittance characteristics of the GDG can be addressed using the CMT [30–32]. Figure 2 shows the two equivalent resonators are named A_1, A_2 as the excitation state modes. The input amplitude of the incident wave and the output amplitude of the reflected wave of the coupler are expressed by $A_{1\pm}^{\mathrm{in}}$, $A_{2\pm}^{\mathrm{in}}$, $A_{1\pm}^{\mathrm{out}}$, and $A_{2\pm}^{\mathrm{out}}$. The A_+ and A_- are used to indicate the direction of propagation at the waveguide, as shown in Fig. 2. The complex amplitude of the two resonators can be expressed as

$$\begin{pmatrix} \gamma_1 & -i\mu_{12} \\ -i\mu_{21} & \gamma_2 \end{pmatrix} \cdot \begin{pmatrix} A_1 \\ A_2 \end{pmatrix} = \begin{pmatrix} \sqrt{\frac{1}{\gamma_{o1}}} & 0 \\ 0 & \sqrt{\frac{1}{\gamma_{o2}}} \end{pmatrix} \cdot \begin{pmatrix} A_{1+}^{in} + A_{1-}^{in} \\ A_{2+}^{in} + A_{2-}^{in} \end{pmatrix}, \tag{2}$$

where $\gamma_1 = (i\omega - i\omega_1 - 1/\gamma_{i1} - \gamma_{o1})$, $\gamma_2 = (i\omega - i\omega_2 - 1/\gamma_{i2} - \gamma_{o2})$, ω is the angular frequency, and $\omega_{1(2)}$ is the

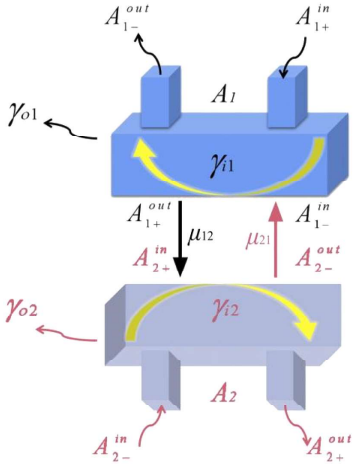

Fig. 2. Equivalent theoretical coupling model of graphene-based plasma resonators.

resonant angular frequency. The μ_{12}, μ_{21} are the coupling coefficients between the two modes, and γ_{i1} and γ_{i2} are the inherent loss of UGG and LGG. According to the conservation of energy, we can get the coupling relationship of the system,

$$A_2^{\text{in}} = A_{1+}^{\text{out}} e^{i\varphi}, \quad A_1^{\text{in}} = A_{1-}^{\text{out}} e^{i\varphi}, \tag{3}$$

$$A_{1+}^{\text{out}} = A_{1+}^{\text{in}} - \sqrt{\frac{1}{\gamma_{o1}}} A_1, \quad A_{1-}^{\text{out}} = A_{1-}^{\text{in}} - \sqrt{\frac{1}{\gamma_{o1}}} A_1, \tag{4}$$

$$A_{2+}^{\text{out}} = A_{2+}^{\text{in}} - \sqrt{\frac{1}{\gamma_{o2}}} A_2, \quad A_{2-}^{\text{out}} = A_{2-}^{\text{in}} - \sqrt{\frac{1}{\gamma_{o2}}} A_2. \tag{5}$$

Here φ represents the phase difference between upper and lower resonators,

$$t = \frac{A_{2+}^{\text{out}}}{A_{1+}^{\text{in}}} = e^{i\varphi} + \left[\gamma_{o1}\gamma_2 e^{i\varphi} + \gamma_o\gamma_1 + \sqrt{\gamma_{o1}\gamma_2}\left(\delta_1 e^{i\varphi} + \delta_2\right)\right] \cdot \sqrt{(\gamma_1\gamma_2 - \delta_1\delta_2)}, \tag{6}$$

where $\delta_1 = i\mu_{12} + e^{i\varphi}\sqrt{(\gamma_{o1}\gamma_{o2})}$, and $\delta_2 = i\mu_{21} + e^{i\varphi}\sqrt{(\gamma_{o1}\gamma_{o2})}$. So, the transmittance that can be deduced is $T = |t|^2$.

3. SIMULATIONS AND RESULTS

To thoroughly comprehend the Fano resonance, we analyze the results to simulate the optical structure and obtain the transmission spectra. Figures 3(a) and 3(c) show the transmission spectra of the UGG and LGG studied. It can be seen from the electric field distribution diagram that when UGG is used, the electric field is mainly concentrated on the upper graphene, and similarly, when LGG is used, the electric field is concentrated on the lower graphene [see Fig. 3(f)]. In this design, the UGG and LGG are directly excited by the incident light resulting in Fano resonance in the infrared band. The Fano resonance is obtained by bright mode–bright mode excitation, as shown in the electric field diagram. As shown by the blue curve in Fig. 3, the extremely strong electric fields are distributed in the inner edges of the upper graphene and on the surface of the lower graphene, generating a blue Fano curve with a resonance peak of 95.7%, and transparent windows appear at 5.88 μm. The theoretical fitting Fano resonance of the transmission spectrum based on CMT fits the simulated result well, as shown in Fig. 3(b).

Furthermore, strong dynamic adjustment property is a very important property for graphene. We take advantage of graphene to adjust the PIT. When the Fermi level of UGG is constant, LGG's Fermi level increases in steps of 0.1 eV, and peak1 has an obvious blueshift performing an excellent modulation, as shown in Fig. 4(a). When the Fermi level of LGG is constant, UGG's Fermi level increases in steps of 0.1 eV, and peak2 has an obvious blueshift performing an excellent modulation. The extinction ratio of the peak2 transmission spectrum

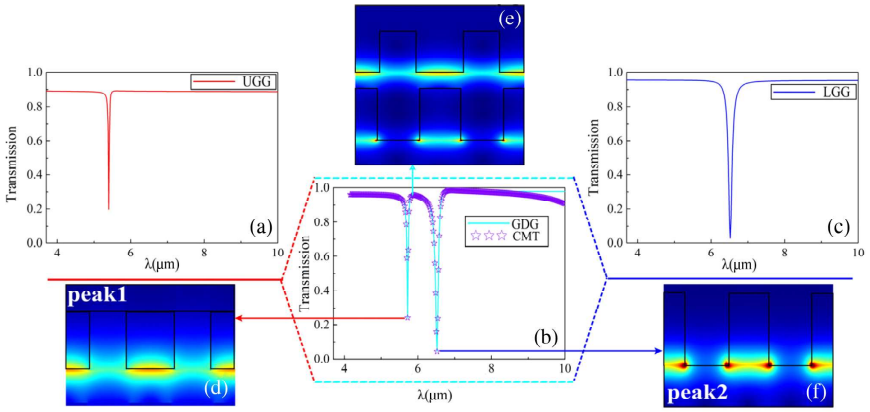

Fig. 3. (a)–(c) Transmission spectra of the UGG, LGG, and GDG; (d)–(f) electric field distribution of the UGG and LGG at the Fano resonance peak. Here, Fermi levels of UGG and LGG are 0.6 and 0.8 eV.

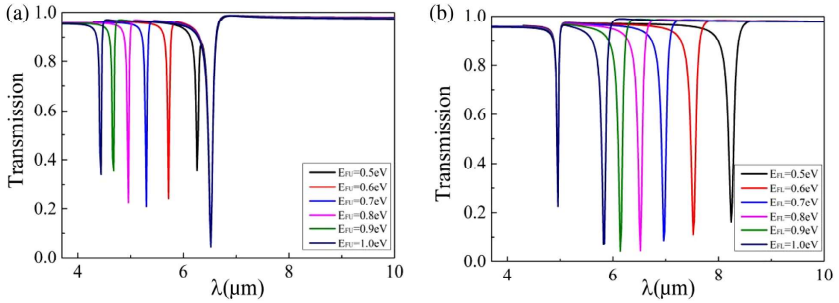

Fig. 4. (a) Transmission spectra of changing the Fermi level of the LGG when $E_{\text{FL}} = 0.8$ eV; (b) transmission spectra of changing the Fermi level of the UGG when $E_{\text{FU}} = 0.8$ eV.

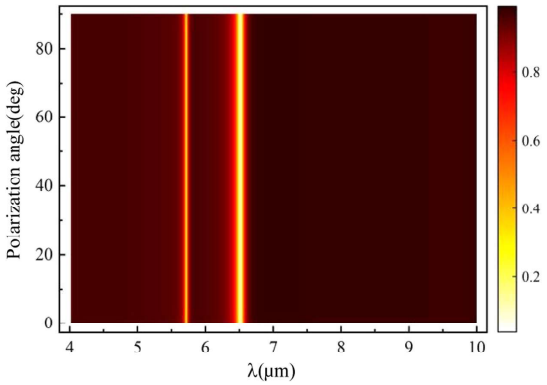

Fig. 5. Transmission spectra as a function of the wavelength and the polarization.

can achieve 96.7% in the range of 0.5–1.0 eV, as shown in Fig. 4(b). This indicates that the Fano system can achieve a superior single-band filter. From the results, it is possible to adjust the wavelength band and range of the transparent window by changing the graphene Fermi levels of UGG and LGG.

We scanned the relationship between polarization angle and transmittance, as shown in Fig. 5, to verify the polarization-independent spectra. Due to the geometric arrangement of the two layers, when the polarization angle θ alters, no matter whether the excitation efficiency of the upper layer increases or decreases, it will be compensated for by the lower layer, making the system polarization-insensitive. From the field distribution diagram, the field distribution of $\theta = 0°$ and $\theta = 90°$ is opposite. As shown in Fig. 6(a), for the case with $\theta = 0°$, the plasmons in the UGG will be excited first and further coupled with the LGG. In contrast, for the case with $\theta = 90°$, the plasmons in the LGG will be excited first and further coupled with the UGG.

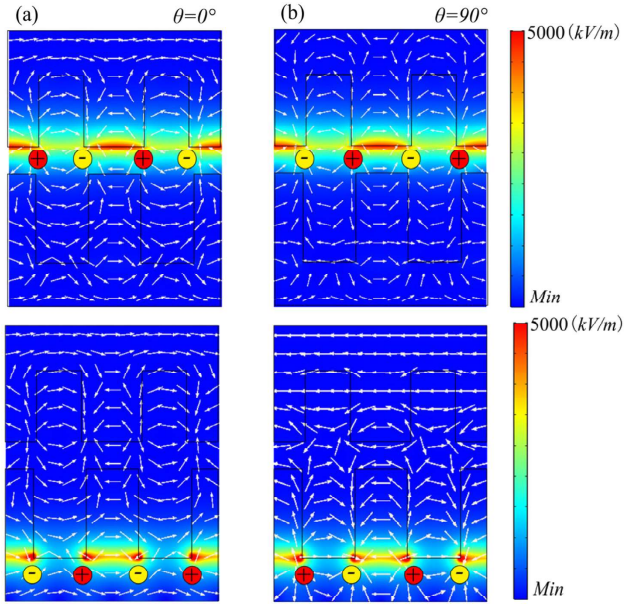

Fig. 6. (a) Spatial distributions of the electric field at polarization angles θ of 0° at 5.72 and 6 μm; (b) spatial distributions of the electric field at polarization angles θ of 90° at 5.72 and 6 μm. Resonant surface charges are represented by "+" and "−"; the more arrows indicate a larger charge density and greater charge density.

Additionally, the Fano system's infrared wave switch can be observed in Fig. 7. Thanks to the unique property of Fano resonance, its transmission will change from maximum to minimum in a very narrow frequency band. We can adjust the Fermi levels of LGG and UGG to obtain electrical switches at different wavelengths, as shown in Figs. 7(a)–7(d). In Fig. 7(a), when the LGG and UGG graphene Fermi level is 0.7 eV, the

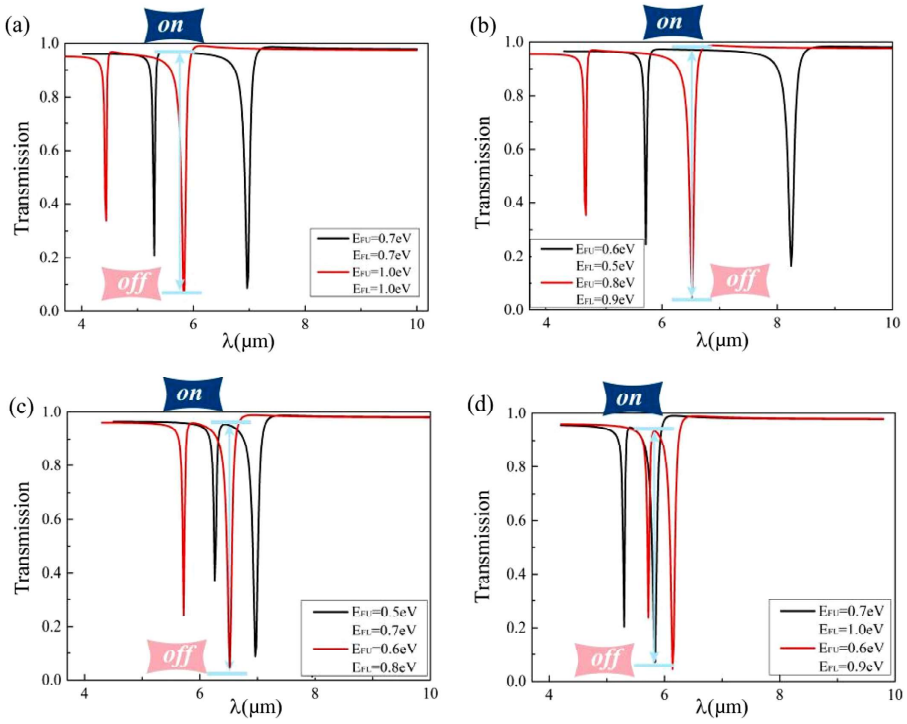

Fig. 7. (a)–(d) Schematic diagram of electro-optical switches at different Fermi levels.

transmission amplitude T_1 at 5.82 μm is 96.6%, meaning transmission loss is 3.4%; when the LGG and UGG graphene Fermi level is 1.0 eV, the transmission amplitude T_2 also at 5.82 μm is 6.7%. We set 96% of the highest transmittance point to "on" and 6.7% of the lowest transmittance point to "off." The modulation degree (M) [33] of amplitude at 5.82 μm can obtain $M = ((T_1 - T_2)/T_1) * 100\% = 93.04\%$. Meanwhile, we also calculated that M at other Fermi levels are equal to 95.43%, 95.28%, and 92.22%. Figure 7 shows the transmission spectra as a function of the wavelength and the Fermi energy, which declares the filtering and switch mechanism. Therefore, two buttons of $E_{FU} = 0.7$ eV, $E_{FL} = 0.7$ eV and $E_{FU} = 1.0$ eV, $E_{FL} = 1.0$ eV can implement a switch of the on/off state, as shown in Fig. 8.

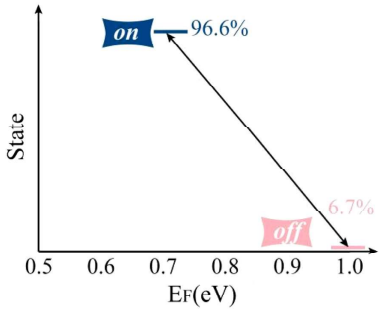

Fig. 8. Switch adjustment diagram when $E_{FU} = E_{FL} = 0.7$ eV and $E_{FU} = E_{FL} = 1.0$ eV.

The evolving relationship between phase shift and group refractive index and wavelength at different Fermi levels in this structure is shown in Fig. 9. It is not difficult to understand. Furthermore, the phase shift and the group refractive index have a corresponding perfect relationship, and both have a sudden change at the Fano resonance. The sudden change can be illustrated as high dispersion. The system's destructive interference can result in high dispersion of the excited plasma wave near Fano resonance. Meanwhile, it induces a distinct phase transition, resulting in a significant change in the group's refractive index. The phase shift and group velocity gradually increase as the Fermi level increases, as shown in Fig. 9. As the LGG Fermi level increases, the group refractive index can reach a maximum of 816. With this feature, the structure has significant application prospects in slow light.

In Fig. 10(a), we show the wavelength shifts of peak1 and peak2 as a function of different dielectric refractive index values.

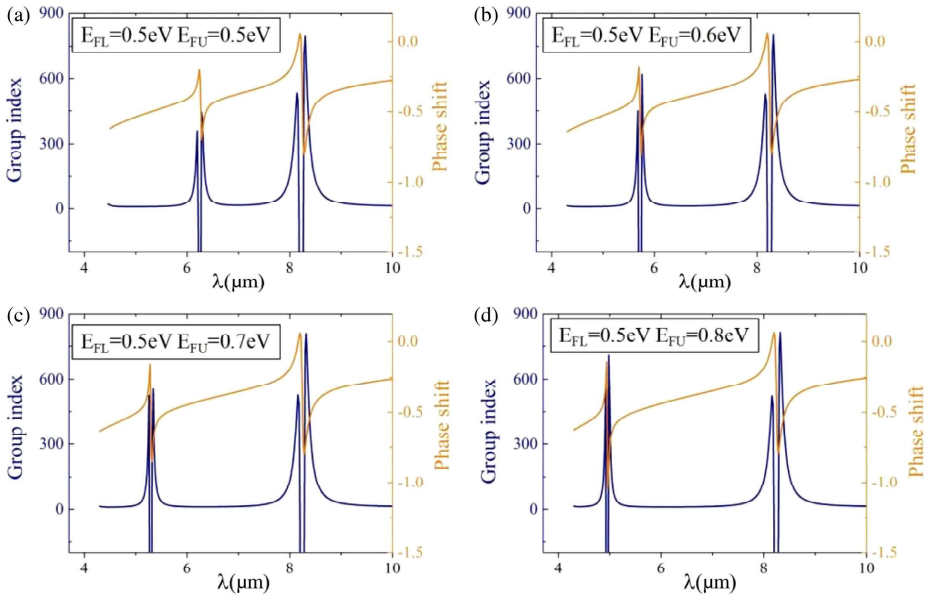

Fig. 9. (a)–(d) Group index (blue lines) and phase shift (orange lines) versus frequency as the Fermi levels $E_{FL} = 0.5$ eV and $E_{FU} = 0.5$ eV, 0.6 eV, 0.6 eV, 0.8 eV, respectively.

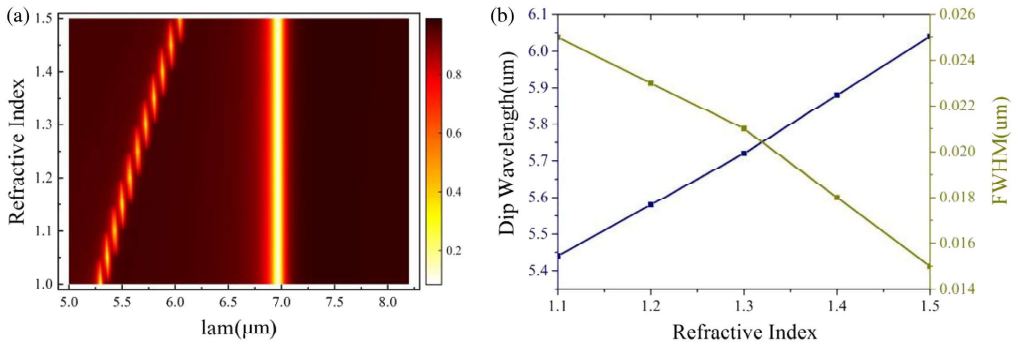

Fig. 10. (a) Three-dimensional modulation diagram of different dielectric refractive index; (b) dip wavelength and FWHM of GDG.

Table 1. Comparison of Our Results and Those Obtained in Recent Studies

Reference	Working Wavelength (μm)	Sensitivity (S) (nm/RIU)	FOM
[35]	1.2–6.0	4650	37
[36]	0.6–1.5	1217	24.34
[37]	1.8–2	1320	17.6
[38]	7.5–10	3400	6.38
This work	5.0–8.5	1600	100

We choose this GDG to investigate its possible applications in sensing. The peak1 resonance wavelength has a linear relationship with the refractive index of the dielectric layer. When the refractive index of the dielectric refractive index increases, the transmission spectra of peak1 exhibit a redshift. From the change in refractive index, peak2 is not sensitive to the change in refractive index. The refractive index sensitivity S is calculated with $S = \Delta lam/\Delta n$ [34]. It is observed that peak1's full width at half-maximum (FWHM) slightly decreases with an increase in the dielectric layer refractive index. At peak1, the spectral S max is 1.6 μm/RIU, and the FOM is 100, as shown in Fig. 10. Table 1 shows a comparison of the sensitivity and FOM of the proposed structure with those obtained in recent studies. The high sensitivity detection platform will have great potential applications in chemical detection, biomolecular sensing, and temperature sensing.

4. CONCLUSIONS

A novel periodic GDG metamaterial structure is built in this paper. We analyze the Fano resonance of the GDG and its applications using advanced simulations with CMT. The electric field distribution is used to explain the formation mechanism of Fano resonance. We found that the GDG can obtain a good tuning performance in different frequency bands and bandwidths using the dynamic adjustment external voltage of graphene. There will be no change in the transmission spectrum of the incident light under these different polarization directions. The results show that the main single-band filter and electro-optical switch with an extinction rate of 95.43% can be realized by adjusting the Fermi level of graphene. Using the group refractive index, sensitivity, and FOM, we have known that this system can achieve a very superior slow-light capability and is a competitive sensor. The maximum group refractive index and FOM can reach about 816 and 100. Thus, this study lays a firm theoretical foundation for completing electro-optical switches, slow light, and sensors.

Funding. Undergraduate Research and Innovation Projects of Jiangnan University (2020366Y); Open Fund of State Key Laboratory of Applied Optics (SKLAO2020001A04); Intergovernmental Science and Technology Regular Meeting Exchange Project of Ministry of Science and Technology of China (CB02-20); National Natural Science Foundation of China (11811530052).

Disclosures. The authors declare no conflicts of interest.

Data Availability. The data that support the findings of this study are available from the corresponding author upon reasonable request.

REFERENCES

1. U. Fano, "Effects of configuration interaction on intensities and phase shifts," Phys. Rev. **124**, 1866–1878 (1961).
2. P. Markoš and V. Kuzmiak, "Coupling between Fano and Bragg bands in the photonic band structure of two-dimensional metallic photonic structures," Phys. Rev. A **94**, 033845 (2016).
3. W. L. Barnes, A. Dereux, and T. W. Ebbesen, "Surface plasmon subwavelength optics," Nature **424**, 824–830 (2003).
4. R. Yu, L. M. Liz-Marzán, and F. J. García De Abajo, "Universal analytical modeling of plasmonic nanoparticles," Chem. Soc. Rev. **46**, 6710–6724 (2017).
5. R. H. Ritchie, "Plasma losses by fast electrons in thin films," Phys. Rev. **106**, 874–881 (1957).
6. T. J. Echtermeyer, S. Milana, U. Sassi, A. Eiden, M. Wu, E. Lidorikis, and A. C. Ferrari, "Surface plasmon polariton graphene photodetectors," Nano Lett. **16**, 8–20 (2015).
7. X. Zhao, L. Zhu, C. Yuan, and J. Yao, "Tunable plasmon-induced transparency in a grating-coupled double-layer graphene hybrid system at far-infrared frequencies," Opt. Lett. **41**, 5470–5473 (2016).
8. S. Kim, M. S. Jang, V. W. Brar, K. W. Mauser, L. Kim, and H. A. Atwater, "Electronically tunable perfect absorption in graphene," Nano Lett. **18**, 971–979 (2018).
9. S. A. de Carvalho and L. E. E. de Araujo, "Electromagnetically-induced phase grating: a coupled-wave theory analysis," Opt. Express **19**, 1936–1944 (2011).
10. S. Zhang, D. A. Genov, Y. Wang, M. Liu, and X. Zhang, "Plasmon-induced transparency in metamaterials," Phys. Rev. Lett. **101**, 218–221 (2008).
11. A. Fallahi and J. Perruisseau-Carrier, "Design of tunable biperiodic graphene metasurfaces," Phys. Rev. B **86**, 195408 (2012).
12. H. Li, L. Wang, J. Liu, Z. Huang, B. Sun, and X. Zhai, "Investigation of the graphene based planar plasmonic filters," Appl. Phys. Lett. **103**, 211104 (2013).
13. T. Kim, H. Kim, R. Zhao, S. S. Oh, T. Ha, D. S. Chung, Y. H. Lee, B. Min, and S. Zhang, "Electrically tunable slow light using graphene metamaterials," ACS Photon. **5**, 1800–1807 (2018).
14. Z. He, H. Li, B. Li, Z. Chen, H. Xu, and M. Zheng, "Theoretical analysis of ultrahigh figure of merit sensing in plasmonic waveguides with a multimode stub," Opt. Lett. **41**, 5206–5209 (2016).
15. H. Cheng, S. Chen, P. Yu, and X. Duan, "Dynamically tunable plasmonically induced transparency in periodically patterned graphene nanostrips," Appl. Phys. Lett. **103**, 203112 (2013).
16. D. A. Smirnova, A. E. Miroshnichenko, Y. S. Kivshar, and A. B. Khanikaev, "Tunable nonlinear graphene metasurfaces," Phys. Rev. B **92**, 161406 (2015).
17. F. Wang, Y. Zhang, C. Tian, C. Girit, A. Zettl, M. Crommie, and Y. R. Shen, "Gate-variable optical transitions in graphene," Science **320**, 206–209 (2008).
18. A. V. Zayats, I. I. Smolyaninov, and A. A. Maradudin, "Nano-optics of surface plasmon polaritons," Phys. Rep. **408**, 131–314 (2005).
19. S. Kim, M. S. Jang, V. W. Brar, Y. Tolstova, K. W. Mauser, and H. A. Atwater, "Electronically tunable extraordinary optical transmission in graphene plasmonic ribbons coupled to subwavelength metallic slit arrays," Nat. Commun. **7**, 12323 (2016).
20. J. Wang, L. Yang, M. Wang, Z. Hu, Q. Deng, Y. Nie, F. Zhang, and T. Sang, "Perfect absorption and strong magnetic polaritons coupling of graphene-based silicon carbide grating cavity structures," J. Phys. D **52**, 15101 (2019).
21. S. Xia, X. Zhai, L. Wang, and S. Wen, "Plasmonically induced transparency in in-plane isotropic and anisotropic 2D materials," Opt. Express **28**, 7980–8002 (2020).
22. T. Bai, Y. Tang, Z. Hu, T. Xing, Z. Lu, Y. Huang, and J. Wang, "High-performance sensitive TE/TM mode switch with graphene-based metal-dielectric resonances," IEEE Sens. J. **21**, 2791–2797 (2021).
23. Z. Bao, J. Wang, Z. Hu, A. Balmakou, S. Khakhomov, Y. Tang, and C. Zhang, "Coordinated multi-band angle insensitive selection absorber based on graphene metamaterials," Opt. Express **27**, 31435–31445 (2019).
24. K. J. Lee, Y. H. Ko, N. Gupta, and R. Magnusson, "Unpolarized resonant notch filters for the 8–12 μm spectral region," Opt. Lett. **45**, 4452–4455 (2020).

25. A. K. Geim and K. S. Novoselov, "The rise of graphene," Nat. Mater. **6**, 183–191 (2007).
26. L. A. Falkovsky, "Optical properties of graphene," J. Phys. Conf. Series **129**, 12004 (2008).
27. C. H. Gan, H. S. Chu, and E. P. Li, "Synthesis of highly confined surface plasmon modes with doped graphene sheets in the mid-infrared and terahertz frequencies," Phys. Rev. B **85**, 117–122 (2012).
28. D. Rodrigo, A. Tittl, O. Limaj, F. J. G. D. Abajo, V. Pruneri, and H. Altug, "Double-layer graphene for enhanced tunable infrared plasmonics," Light Sci. Appl. **6**, e16277 (2017).
29. Z. Fang, S. Thongrattanasiri, A. Schlather, Z. Liu, L. Ma, Y. Wang, P. M. Ajayan, P. Nordlander, N. J. Halas, and F. J. García De Abajo, "Gated tunability and hybridization of localized plasmons in nanostructured graphene," ACS Nano **7**, 2388–2395 (2013).
30. H. Xu, H. Li, B. Li, Z. He, Z. Chen, and M. Zheng, "Influential and theoretical analysis of nano-defect in the stub resonator," Sci. Rep. **6**, 30877 (2016).
31. A. H. Haus and W. Huang, "Coupled-mode theory," Proc. IEEE **79**, 1505–1518 (1991).
32. K. L. Tsakmakidis, L. Shen, S. A. Schulz, X. Zheng, J. Upham, X. Deng, H. Altug, A. F. Vakakis, and R. W. Boyd, "Breaking Lorentz reciprocity to overcome the time-bandwidth limit in physics and engineering," Science **356**, 1260–1264 (2017).
33. Z. Liu, E. Gao, X. Zhang, H. Li, H. Xu, Z. Zhang, X. Luo, and F. Zhou, "Terahertz electro-optical multi-functional modulator and its coupling mechanisms based on upper-layer double graphene ribbons and lower-layer a graphene strip," New J. Phys. **22**, 53039 (2020).
34. M. Mehdi Keshavarz and A. Alighanbari, "Terahertz refractive index sensor based on Tamm plasmon-polaritons with graphene," Appl. Opt. **58**, 3604–3612 (2019).
35. M. R. Rakhshani and M. A. Mansouri-Birjandi, "A high-sensitivity sensor based on three-dimensional metal–insulator–metal racetrack resonator and application for hemoglobin detection," Photon. Nanostr. Fundam. Appl. **32**, 28–34 (2018).
36. E. Rafiee, R. Negahdari, and F. Emami, "Plasmonic multi channel filter based on split ring resonators: application to photothermal therapy," Photon. Nanostr. Fundam. Appl. **33**, 21–28 (2019).
37. M. J. Al-mahmod, R. Hyder, and M. Z. Islam, "Numerical studies on a plasmonic temperature nanosensor based on a metal-insulator-metal ring resonator structure for optical integrated circuit applications," Photon. Nanostr. Fundam. Appl. **25**, 52–57 (2017).
38. X. Yan, L. Yuan, Y. Wang, T. Sang, and G. Yang, "Transmittance characteristics and tunable sensor performances of plasmonic graphene ribbons," AIP Adv. **6**, 85301 (2016).